Comput Mech
DOI 10.1007/s00466-014-1090-5

ORIGINAL PAPER

Experimental and numerical FSI study of compliant hydrofoils

B. Augier · J. Yan · A. Korobenko · J. Czarnowski · G. Ketterman · Y. Bazilevs

Received: 27 September 2014 / Accepted: 16 October 2014

Abstract A propulsion system based on tandem hydrofoils is studied experimentally and numerically. An experimental measurement system is developed to extract hydrodynamic loads on the foils and capture their twisting deformation during operation. The measured data allowed us to assess the efficiency of the propulsion system as a function of travel speed and stroke frequency. The numerical simulation of the propulsion system is also presented and involves 3D, full-scale fluid–structure interaction (FSI) computation of a single (forward) foil. The foil is modeled as a combination of the isogeometric rotation-free Kirchhoff–Love shell and bending-stabilized cable, while the hydrodynamics makes use of the finite-element-based arbitrary Lagrangian–Eulerian variational multiscale formulation. The large added mass is handled through a quasi-direct FSI coupling technique. The measurement data collected is used in the validation of the FSI simulation, and excellent agreement is achieved between the predicted and measured hydrodynamic loads and foil twisting motion.

Keywords Propulsion · Thrust · Compliant hydrofoils · Fluid–structure interaction · Isogeometric analysis · ALE–VMS

B. Augier · J. Yan · A. Korobenko · Y. Bazilevs (✉)
Department of Structural Engineering, University of California, San Diego, 9500 Gilman Drive, Mail Code 0085, La Jolla, CA 92093, USA
e-mail: yuri@ucsd.edu

J. Czarnowski · G. Ketterman
Hobie Cat Company, 4925 Oceanside Blvd., Oceanside, CA 92056, USA

1 Introduction

It is now well understood that the details of the structural geometry and motions (e.g., the shape of insect wings and their flapping patterns) have a significant effect on the dynamics of the surrounding flow, and the lift and thrust performance of a propulsive system [20]. As a result, in order to have a well designed propulsive system, geometry, materials, and motion actuation techniques need to be carefully selected. Many designs make use the so-called 'bioinspired' or 'biomimetic' concept, which is based on the assumption that insects, birds, or fish, over the span of their evolution, have developed the wing shape, structure, and motion that lead to optimized propulsion in aerodynamic or hydrodynamic environments (see, e.g., [23,40,45,49,50,53,57,58]). Recent examples that use bioispired design concepts may be found in [53,59,74] for Micro Aerial Vehicles and in [22,37] for optimized placement of Vertical-Axis Wind Turbines in arrays.

In the present paper we undertake a combined experimental and computational fluid–structure interaction (FSI) investigation of a bioinspired propulsion system that makes use of tandem compliant hydrofoils. There is an extensive literature on experimental thrust generation studies for pitching, heaving, and combined motions of individual foils (see, e.g., [36,39,48]). In [20] the authors have examined the effects of both the foil morphology and motion on thrust generation and propulsion efficiency. In these studies the foils were either rigid or had significantly reduced complexity of the geometry and structural design. A tandem propulsion configuration was studied experimentally in [90,91] for the flight of a dragon fly, focusing on details of aerodynamics, flight efficiency, and interaction of the forward and hind wing of the insect. Recent work on the locust flight in [53,57,58] and MAV flight with locust wings in [53,59,74] produced

Published online: 09 November 2014

state-of-the-art moving-domain simulations that were able to capture in detail and with excellent accuracy the underlying aerodynamics phenomena, including the interaction of the locust forward and hind wings. In the present work, although the tandem foil configuration is employed, we focus on the measurements and prediction, using FSI, of hydrodynamic loads and deformations for a single (forward) foil. However, we do so in 3D, at full scale, under actual operating conditions, and considering full complexity of the foil structural design and the underlying hydrodynamics phenomena.

Several challenges are present in hydrofoil FSI: a. The flow Reynolds number is high resulting in wall-bounded turbulent flow with thin boundary layers that need appropriate numerical treatment by means of boundary-layer meshing and weakly-enforced essential boundary conditions [11,14,15,25]; b. The relative mass of the foils is small leading to high added mass in the coupled FSI problem that, in turn, requires a so-called quasi-direct solution technique [81–83,85] to achieve convergence of the solution of the coupled equation system; c. The foils are quite flexible and undergo large motions and deformations during operation, which requires an accurate and robust structural mechanics formulation [34,35,38,47] and mesh handling techniques [32,51,78–81]. These challenges are similar to those involved in other categories of FSI problems [16], such as the spacecraft aerodynamics [61], FSI modeling of spacecraft parachutes [60,64,67,69,70,73,77], sails [1,2,84], cardiovascular fluid mechanics and FSI [5,9,10,27,42,52,53,55,63,65,71,72,76], and pulsatile ventricular assist devices [41,43,44], and are addressed in this paper in order to carry out the hydrofoil FSI simulations.

The paper is comprised of the following parts. In Sect. 2 we describe the propulsion system studied, and the experimental measurement system and techniques devised for this purpose. We then present unsteady hydrodynamic load and foil deformation measurements, and quantify the propulsion system efficiency for different travel speeds. In Sect. 3 we briefly describe the numerical methods employed, construct and validate the structural model of the foil, and present an FSI simulation focusing on the comparison between the predicted and measured foil load and deformation data. In Sect. 4 we draw conclusions.

2 Experimental investigation of the propulsion system

In this section we describe the inner workings of the propulsion system analyzed, which is the Mirage Drive designed and built by Hobie Cat Co. We then provide some details on the measurement system devised to study hydrodynamic loading on the foils and their twisting deformation. The dynamic loading measurements obtained are presented next, and, using this data, propulsive efficiency of the Mirage Drive as a function of travel speed and stroke frequency is assessed.

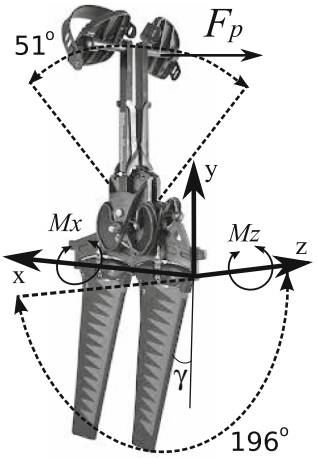

Fig. 1 Mirage Drive propulsion system

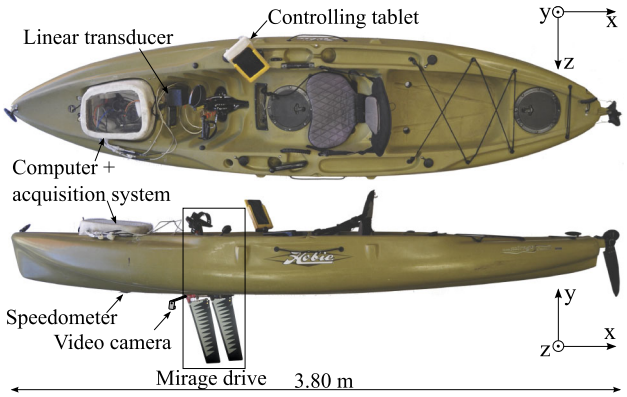

Fig. 2 Instrumented kayak equipped with the Mirage Drive

2.1 Mirage Drive propulsion system

The Mirage Drive is a human-powered propulsion system that transforms pedaling motion of a driver into transverse sweeping motion of two underwater foils (see Fig. 1 for a depiction of the Mirage Drive propulsion system). The propulsion system is typically installed on surface vessels used for recreational water-sports activities, such as kayaking. The system is installed by inserting it through the boat hull such that the foils protrude beneath the hull, and the pedals are accessible to the driver atop the boat (see Fig. 2). The foils are placed in a tandem configuration and sweep through an angle of 196°.

As the driver pedals, the foils move under water. The periodic motion of each foil is dominated by rigid-body rotation induced by that of the main steel shaft (or mast) located at the foil's leading edge. The rigid body rotation takes place along the axis aligned with the direction of travel of the vessel. The compliant nature of the foils also results in significant twist-

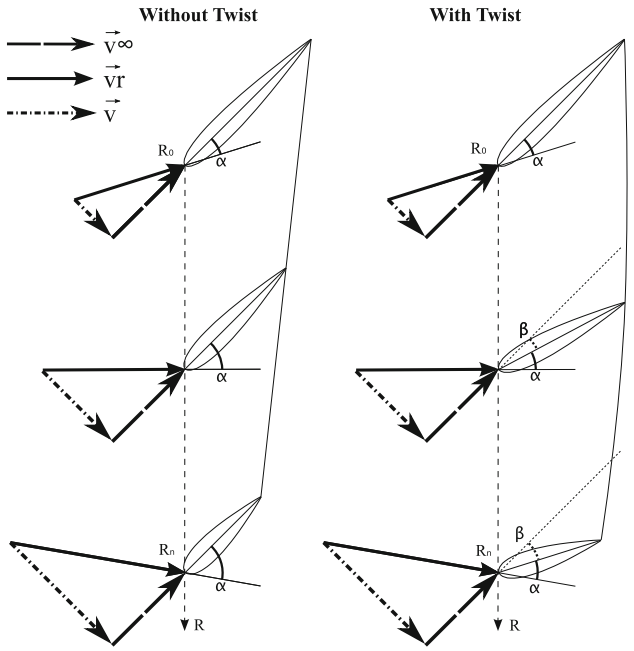

Fig. 3 Illustration of the apparent flow angle α and twist angle β. In the absence of twisting $\beta = 0$

ing and somewhat less pronounced bending motion of the foil's axial cross-sections. It is precisely this additional elastic deformation of the foils that generates the necessary thrust force that propels the vessel forward. The foil motion and its compliant nature bring about space- and time-dependent variation of the apparent flow angle α and twist angle β (see Fig. 3 for an illustration). In the absence of twisting (i.e., $\beta = 0$) no thrust can be generated, while very large values of β may lead to excessive drag. As a result, it is desirable to design the foil geometry and materials (i.e., stiffness) such that, when the foil is loaded with hydrodynamic forces, the fraction of the pedaling effort that goes into the resulting thrust force is maximized. However, even before such optimization studies are performed, it is important to devise an experimental apparatus, coupled to an advanced FSI model of the propulsion system to understand its behavior in typical operating conditions.

2.2 Measurement system

Full-scale measurements are performed on a Outback kayak (see Fig. 2) also built by the Hobie Cat Co. The Outback is a 3.80 m, 40 kg fully rigged kayak made of rotomolded Polyethylene with the Mirage Drive propulsion system installed. The kayak and propulsion system are equipped with dedicated instrumentation, and the following measurements are performed:

– Moments in the x- and z-direction created by the hydrodynamic forces, denoted by M_x and M_z, respectively,

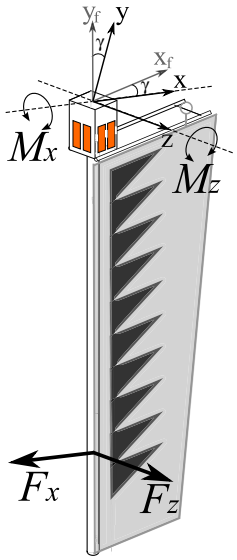

Fig. 4 Positioning of the gauges and coordinate system employed

are measured using two 120 ohm gauges (HBM LY11-3/120) mounted in a Wheastone bridge configuration. The mast insert is replaced by a stainless steel square bar. The gauges are placed on the square bar, and the bar is welded on the shaft, drilled, and threaded to screw in the mast. We refer to this setup as the hydrodynamic balance. Figure 4 illustrates the position of the gauges on each face of the square bar, as well as the coordinate frames used in the study. We assume that the y- and z-axes rotate with the mast, and the x-axis is coincident with the kayak direction of travel (see Fig. 2). Note that M_z is generated by the thrust force, while M_x arises due to the lateral forces acting on the foil. As a result, a good foil design may be characterized as having a larger M_z-to-M_y ratio. Also note that different masts can be attached to the stainless steel bar, which facilitates testing many different designs using the same hydrodynamic balance system.

– The bracket of the left pedal is instrumented in order to measure the time-dependent force applied by the driver. The load sensors are connected to a dedicated gauge analog amplifier and conditioner Expresso from HBM. The position of the pedal is measured by a linear transducer attached from the inside of the cockpit to the right bracket. The linear transducer is linked to a Dataq 430 AD converter.
– The kayak speed is measured by a trough-the-hull speedometer installed on the kayak. The speed signal is recorded via a dedicated NMEA frame converter. Kayak speed is also recorded using a separate GPS device.
– A video camera is installed under the hull of the boat in order to capture the motion of the forward foil. A GoPro Hero3 camera and its supporting bar are attached to the base of the mast of the forward foil. The camera fol-

lows the motion of the mast by rotating with it. Stripes are superposed on the foil snapshots at 30, 60, 80, and 100 % of the span. Their intersection with the leading and trailing edge are marked by lines. Along the stripes, the foil is equipped with so-called telltales located at 15 and 85 % of the chord. This setup allows us to accurately measure the time-dependent twist angle at the locations along the mast where the stripes are placed. Due to the relatively short focal length of the camera there is some distortion that is present in the image making direct post-processing of the twist angle inaccurate. This inaccuracy is overcome with a simple calibration procedure using snapshots of the foil twisted by a prescribed set of angles at each axial cross-section. With this calibration procedure in place, we are able to measure twist angle with 1° precision.

The different instruments employed in the measurements are connected to a inboard PC. Synchronization of the heterogeneous data is done in postprocessing. The load sensors are calibrated to a precision error of < 1 %. Because the tests are done in seawater, appropriate measures are taken to protect the sensors from water damage.

2.3 Dynamic load measurements

The experimental tests presented in this section are done using a set of constant kayak speeds denoted by v_∞. The driver adapts a stroke frequency (or cadence) and the pedal load for different targeted kayak speeds. The following cases are tested corresponding to different cruising conditions:

- $v_\infty = 1.44$ m/s: Low-speed cruising,
- $v_\infty = 1.75$ m/s: Medium-speed cruising,
- $v_\infty = 2.11$ m/s: High-speed cruising,
- $v_\infty = 2.52$ m/s: Competitive racing.

The driver keeps a steady speed for 60 s while the measurement data is recorded. Figure 5 shows the time history of the applied force perpendicular to the pedal axis at different kayak speeds. Angular position of the pedal is periodic in time and may be closely approximated by a sine function, the fact which we employ in the computation presented later in the paper. Time history of the pedal force exhibits a steep ramp-up followed by a smoother decay. Note that the driver always applies a positive force on the pedal (i.e., the force vector does not change direction). Figure 6 shows the time series of the moments M_x and M_z acting on the foil at different kayak speeds. Some asymmetry is observed between the positive and negative peaks of M_x for the low-speed cruising case, which is consistent with the driver reporting some difficulties in maintaining this low constant kayak speed. The asymmetry in M_x disappears at higher cruising speeds, which

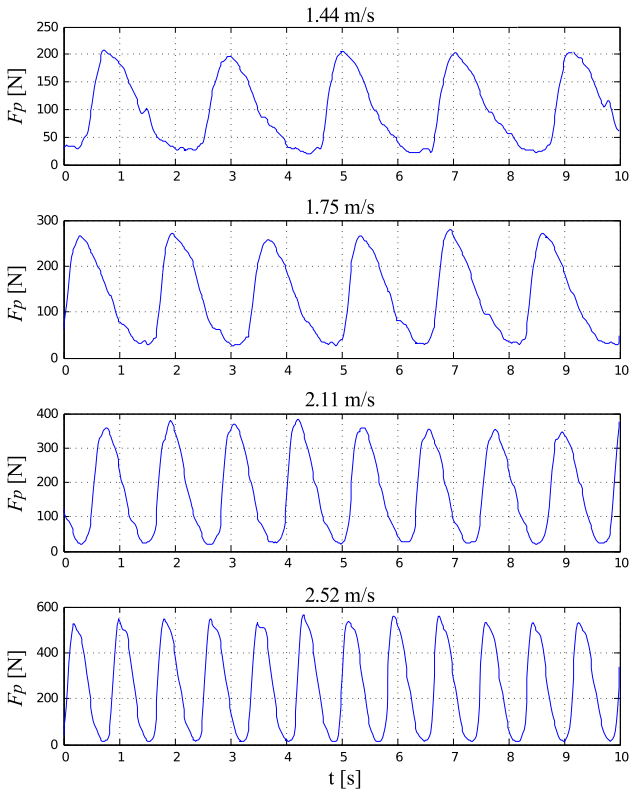

Fig. 5 Times series of the applied pedal force for different kayak speeds

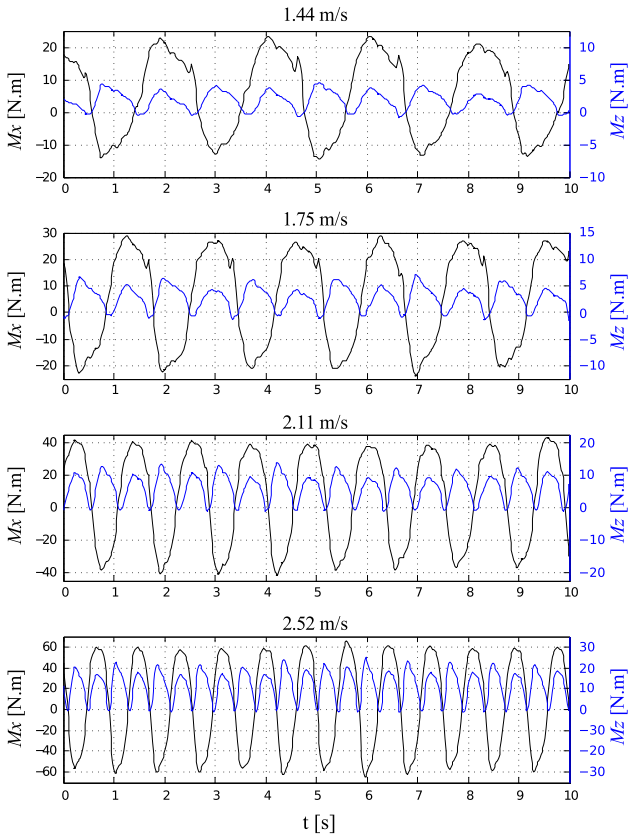

Fig. 6 Times series of M_x and M_z for different kayak speeds

Table 1 Stroke frequency f, efficiency η, and Mz/Mx, the ratio of the maximum moment corresponding to the propulsive force to that corresponding to the foil side force not contributing to thrust

v_∞ (m/s)	1.44	1.75	2.11	2.52
f (Hz)	0.517	0.624	0.750	0.855
η	0.290	0.381	0.458	0.592
Mz/Mx	0.188	0.231	0.335	0.374

The results are summarized for different kayak speeds v_∞

were simpler to maintain in the tests performed. The peaks of M_x and M_z are coincident, meaning the trust force is maximum when the foil side load is maximum, both corresponding to the configuration where the foil is orthogonal to the water surface.

2.4 Efficiency of the propulsion system

We define the propulsion system efficiency η as the ratio

$$\eta = \frac{\bar{P}_{out}}{2\bar{P}_{in}}, \tag{1}$$

where $\bar{P}_{out}$ and $\bar{P}_{in}$ are the average power out and in, respectively. Here $\bar{P}_{out}$ is defined as power required to overcome the boat drag, that is,

$$\bar{P}_{out} = v_\infty \bar{F}_d, \tag{2}$$

where $\bar{F}_d$ is the average boat drag force measured and reported in [46]. The average power $\bar{P}_{in}$ is defined as that exerted by the driver pushing on the pedal, and may be expressed as

$$\bar{P}_{in} = \frac{1}{T}\int_T F_p l\dot{\theta}\, dT, \tag{3}$$

where F_p is the time history of the pedal force shown in Fig. 5, l is the moment arm (distance from the load sensor to the pedal axis), and $\dot{\theta}$ is the time-dependent angular velocity of the pedal. The factor two in the denominator Eq. (1) is due to the fact that there are two pedals.

Table 1 summarizes the boat speed, stroke frequency, and efficiency for the four boat speeds considered.

Efficiency η is also plotted as a function of boat speed and stroke frequency in Fig. 7. The measurement data suggest that the efficiency is nearly a linear function of the boat speed and stroke frequency in the range of boat speeds and stroke frequencies considered. This linear increase in efficiency with boat speed (and stroke frequency) is likely an intrinsic property of foil-based propulsion systems. Table 1 also provides the ratio Mz/Mx, which is the ratio of the maximum moment corresponding to the propulsive force to that corresponding to the foil side force not contributing to thrust. The ratio grows as a function of speed suggesting larger and larger fraction

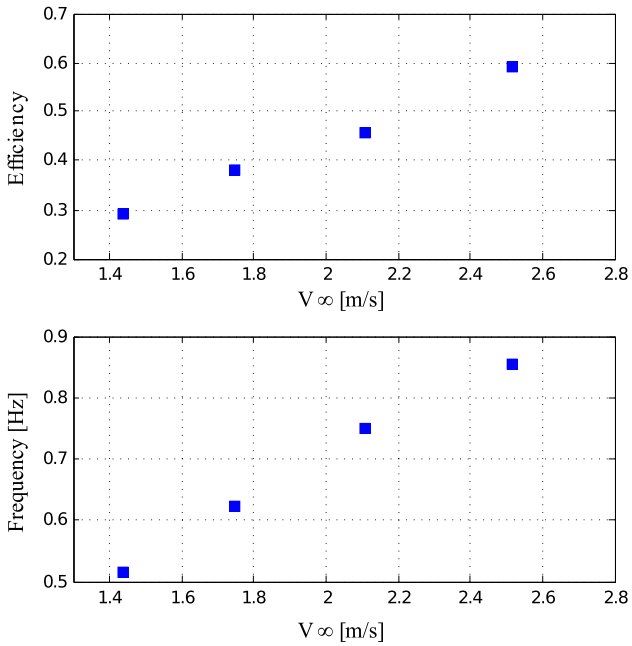

Fig. 7 Efficiency of the propulsion system as a function of boat speed and stroke frequency. Efficiency is nearly a linear function of the boat speed and stroke frequency within the range of parameters considered

of the total effort goes into propelling the kayak forward as the boat speed is increased.

The propulsion system efficiency may be further increased by improving foil geometry and material composition. As a result, besides accurate experimental measurements, it is desirable to develop advanced FSI modeling and simulation methods for such propulsion systems, which is the focus of the following section.

3 FSI simulation of the Mirage Drive

In this section we briefly recall the FSI methods employed in this work. We then develop and validate the foil structural model. We conclude the section by presenting the FSI simulation for one of the kayak speeds reported in the tests above, and show comparison between the experimental and computational results.

3.1 FSI modeling framework and methods

To perform the foil simulation, the FSI framework developed in [7] is employed. At the continuum level, the hydrodynamics of the foil is governed by the Navier–Stokes equations of incompressible flows posed on a moving spatial domain, and written in the Arbitrary Lagrangian–Eulerian (ALE) frame [30]. The governing equations of structural mechanics are written in the Lagrangian frame [18], and consist of the local balance of linear momentum. At the fluid-

structure interface, compatibility of the kinematics and tractions is enforced, namely,

$$\mathbf{u} - \frac{\mathrm{d}\mathbf{y}}{\mathrm{d}t} = \mathbf{0}, \tag{4}$$

$$\boldsymbol{\sigma}_1 \mathbf{n}_1 + \boldsymbol{\sigma}_2 \mathbf{n}_2 = \mathbf{0}, \tag{5}$$

where $\mathbf{u}$ is the fluid velocity, $\frac{\mathrm{d}\mathbf{y}}{\mathrm{d}t}$ is the structural displacement rate, $\boldsymbol{\sigma}_1$ and $\boldsymbol{\sigma}_2$ are the fluid and structure Cauchy stress, respectively, and $\mathbf{n}_1$ and $\mathbf{n}_2$ are the unit outward normal vectors to the fluid and structural mechanics domain, respectively, at their interface.

At the discrete level, the fluid mechanics equations are approximated using the FEM-based ALE–VMS approach [8,54] augmented with weakly enforced boundary conditions [11,14,15]. The former acts as a Large-Eddy Simulation (LES) turbulence model, while the latter relaxes the mesh size requirements in the boundary layer without the loss solution accuracy. ALE–VMS was successfully employed for FSI simulations of wind turbines in [4,6,7,13,24–26,28,37,38]. The structural mechanics modeling is based on a combination of isogeometric rotation-free Kirchhoff–Love shells [34,35] and bending-stabilized cables [47], discretized using Non-Uniform Rational B-Splines (NURBS) [21,29]. This approach gives a good combination of structural-mechanics accuracy due to the higher-order and higher-continuity representation of the geometry and solution, and efficiency due to the lack of rotational degrees of freedom in the formulation. The FSI modeling employed here makes use of a non-matching discretization of the interface between the fluid and structure subdomains. Nonmatching discretizations require interpolation or projection of kinematic and traction data between the nonmatching surface meshes [7,17,54,56,62,66,68,81,84,86–89], which is what we do here.

Having good boundary-layer mesh resolution is critical for hydrodynamics accuracy in the present application, which motivates the use of a moving-mesh technique as opposed to its fixed-grid counterpart. To accommodate the large foil displacements and maintain good mesh quality, the mesh moving is accomplished using a combination of rigid-body motion and elastostatics techniques. The latter is combined with Jacobian-based stiffening, which protects boundary-layer elements from excessive distortion [32,51,78–81].

The generalized-α technique [3,19,31] is used to advance the FSI equations in time. The full discretization of the FSI formulation described above leads to three coupled, nonlinear equations systems, which correspond to the fluid, structure, and mesh parts of the problem, and which need to be solved at every time step. The added mass effect is significant in this problem, necessitating the use of a quasi-direct coupling technique [81–83,85].

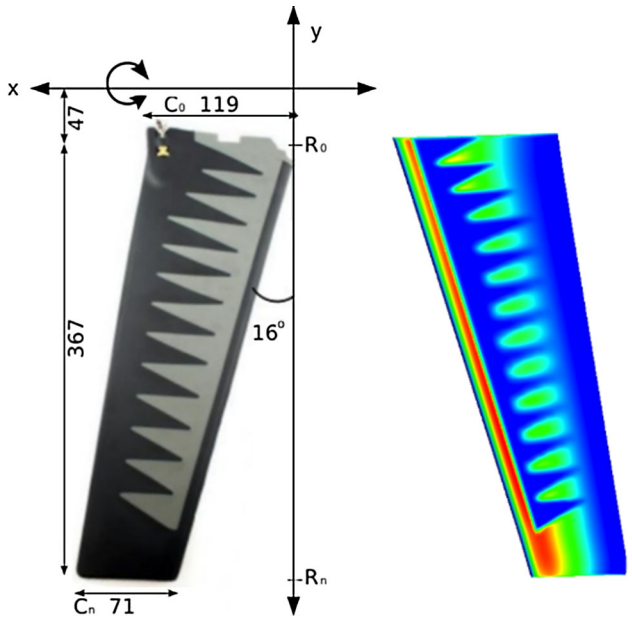

Fig. 8 *Left* Geometry and dimensions of the foil (in mm). *Right* Chordwise bending stiffness distribution

Table 2 Material properties of the foil

Material	Black	Grey
Young's modulus (MPa)	27.58	12.24
Poisson's ratio	0.47	0.47
Density (kg/m^3)	1200	1200

For more details about the various constituents of the FSI formulation employed here, as well as similar methods and techniques, the reader is referred to [17].

3.2 Structural modeling and validation

Figure 8 shows the geometry and dimensions of the foil used in the Mirage Drive propulsion system. The structure has a symmetric hydrofoil shape. Nearly 10,000 quadratic NURBS elements are employed in the model. The model is comprised of two material zones, referred to as "Black" and "Grey" material, as shown on Fig. 8. Each zone is made of an isotropic St. Venant–Kirchhoff material with properties summarized in Table 2. The "zigzag" pattern of the material is designed such that the foil has the desired flexibility and stiffness. The chordwise bending stiffness distribution on the foil surface is presented in Fig. 8, where the zigzag pattern is clearly visible.

To validate the structural model (i.e., to ensure that the geometry and material distribution are correctly assigned) we perform the "sag test" of the foil. The setup is presented in Fig. 9. The foil is clamped in close proximity of the root, and subjected to gravitational force due to its weight. For the purposes of the test, the main shaft is removed from the

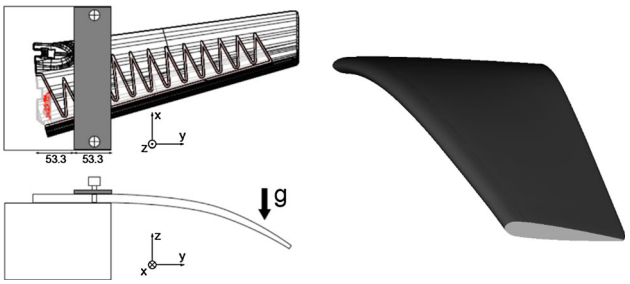

Fig. 9 *Left* Sag test setup. *Right* Deformed shape

Table 3 The "sag test": Comparison of the structural mechanics computation with the lab test results

	Computation	Lab test
Mass (kg)	0.258	0.260
Max deflection (mm)	90.2	87.6
Twist angle (°)	11.0	12.0

structure. The test results are summarized in Table 3. The maximum deflection, twist angle at the tip, and total mass of the foil are compared to the test data and show good agreement. The deformed shape of the foil under gravity is shown in Fig. 9, where the tip deflection and twist are clearly visible.

3.3 FSI problem setup

The computation presented in this section is performed using a single oscillating foil. The two-foil case may be computed with the aid of techniques such as the sliding-interface formulation [12,26,28], or using occasional remeshing in the region between the foils (see, e.g., [53,57,58,75]).

The problem domain is as follows. The outer cylindrical fluid mechanics domain has the radius of 0.96 m and length of 2 m. The foil is placed inside the cylindrical domain as shown in Fig. 10. A uniform inflow velocity of 2.11 m/s corresponding to the high-speed cruising case is set on the inlet plane. On the cylinder lateral surface zero streamwise traction is applied, while the remaining velocity components are set to zero. Finally, at the outflow, zero traction (or "do nothing") boundary conditions are set.

The fluid mechanics mesh uses linear elements, and has triangular prisms in the foil boundary layer and tetrahedra elsewhere in the domain. The boundary-layer mesh is constructed using ten layers of elements, with the size of the first element in the wall-normal direction of 0.0002 m and a growth ratio of 1.2. An inner refinement box is build around the foil in order to better capture the turbulent wake. The fluid mechanics mesh statistics are summarized in Tables 4 and 5. A slice of the fluid mechanics mesh and triangular-prism discretization of the foil boundary layer are shown in Fig. 11.

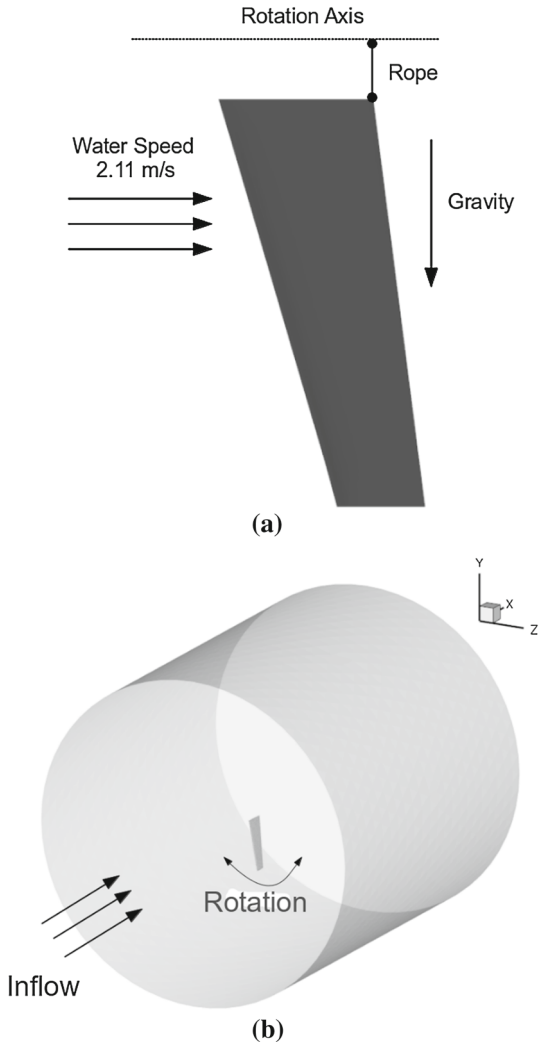

Fig. 10 **a** Initial configuration of the foil; **b** FSI problem domain and setup

Table 4 Mesh sizes (in m) employed in the fluid mechanics domain. Here, "Surface" gives the element in-plane dimension on the foil surface, "Layer" gives the size of the first boundary-layer element in the direction normal to the foil surface, "Inner" gives the mesh size on the surfaces of the inner box used for mesh refinement near the foil, and "Outer" gives the mesh size on the outer cylindrical boundary

Surface	Layer	Inner	Outer
0.003	0.0002	0.015	0.1

Table 5 Number of nodes and elements in the fluid mechanics mesh

Nodes	Elements
485,317	2,275,660

To drive the foil, the following time-dependent kinematic boundary conditions are applied to the leading-edge control points of the foil NURBS mesh:

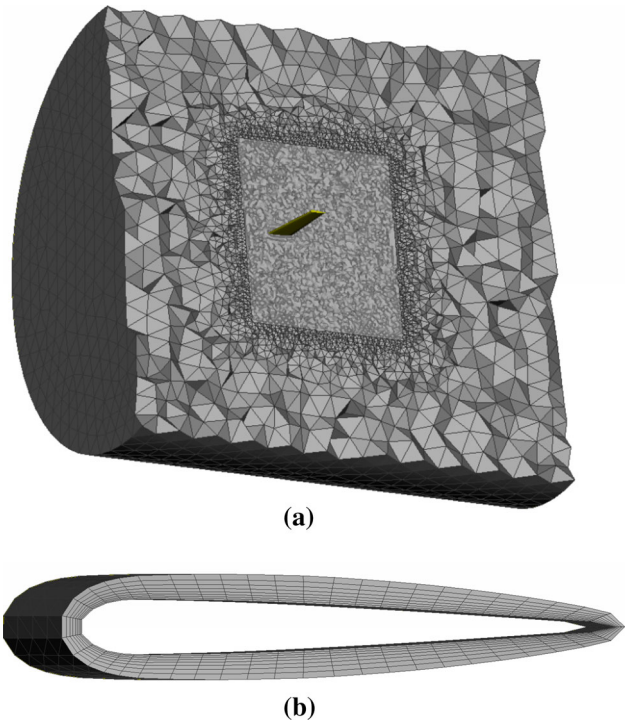

Fig. 11 **a** Slice of the fluid mechanics mesh showing the outer cylinder, inner box, and foil surface. **b** Triangular-prism discretization of the foil boundary layer

$$\theta = \frac{A\pi}{2} \sin\left(\frac{2\pi t}{T}\right), \tag{6}$$

$$\mathbf{y} = (\mathbf{R}(\theta) - \mathbf{I})(\mathbf{X} - \mathbf{X}_0), \tag{7}$$

where $\mathbf{R}(\theta)$ is the rotation matrix, $\mathbf{X}$ denotes the position of the foil leading-edge control points, and $\mathbf{X}_0$ is the center of rotation. In Eq. (6), $\frac{A\pi}{2}$ and T give the maximum rotation angle and period of the oscillation (inverse of the stroke frequency), respectively. In the simulation, we set $A = 1.092$ and $T = 1.154$ s, which are consistent with the high-speed cruising setup. Application of the rigid-body motion models the effect of the steel shaft driving the foil at the leading edge. The top corner of the trailing edge is attached to the rotation axis using a single NURBS cable element (see Fig. 10). This models the actual connection between the trailing edge and rotation axis, intentionally designed to allow the foil to develop higher twisting angles. The cable is slightly loosened to allow mild trailing-edge-top-corner displacement, which, in turn, leads to higher overall foil twist.

The fluid mesh on the foil leading edge and the outer cylinder boundary follows the rigid-body motion given by Eqs. (6) and (7). The fluid mesh on the remainder of foil surface follows the motion of the elastic foil structure. Elsewhere in the domain the mesh displacement is governed by the equations of elastostatics with Jacobian-based stiffening.

The computation is carried out in a parallel computing environment. The mesh is partitioned into subdomains using METIS [33], and each subdomain is assigned to a compute core. The parallel implementation of the methodology may be found in [24]. The time step is set to 1.0×10^{-4} s.

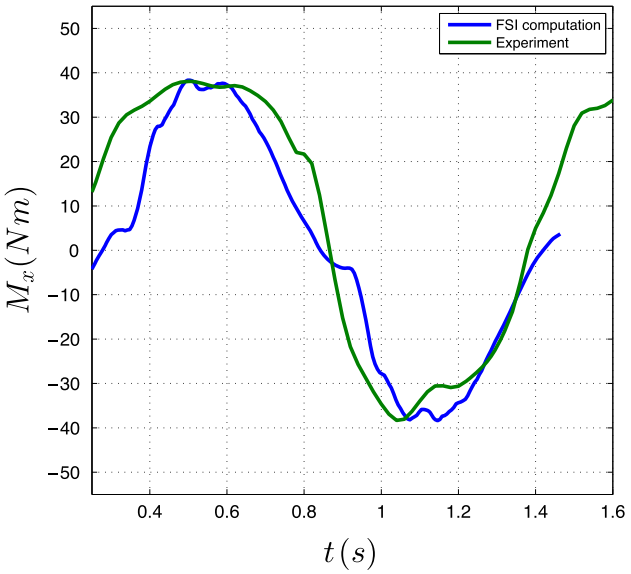

Fig. 12 Time history of M_x. Computational and experimental data are plotted for comparison

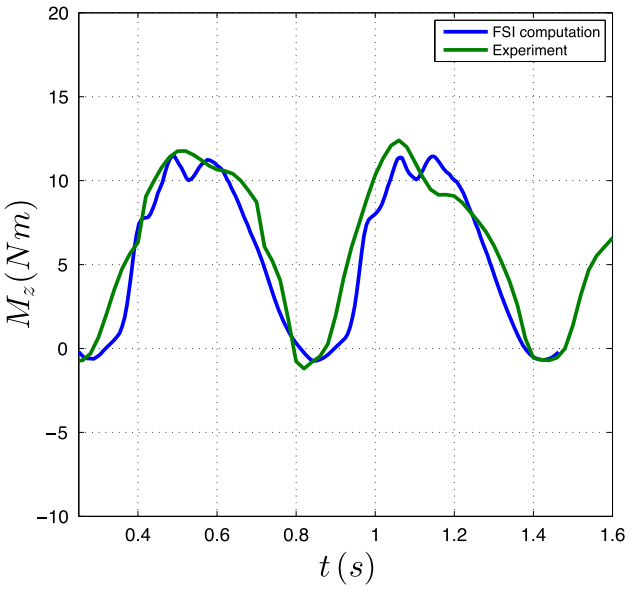

Fig. 13 Time history of M_z. Computational and experimental data are plotted for comparison

3.4 FSI simulation results

Starting with the foil in the underformed configuration, we compute for two stroke cycles. We extract time histories of M_x and M_z from the second cycle and plot them in Figs. 12 and 13, respectively. The maximum predicted M_x is about 41 Nm, while the maximum predicted M_z is about 13 Nm.

Table 6 Comparison of drag and twist angle between the experimental measurements and FSI computation

	Computation	Experiment
Drag (N)	25.53	25.66
Sec. 1 Max. Angle (°)	23.30	22.00
Sec. 2 Max. Angle (°)	29.93	29.00
Sec. 3 Max. Angle (°)	37.32	40.00
Sec. 4 Max. Angle (°)	37.56	40.00

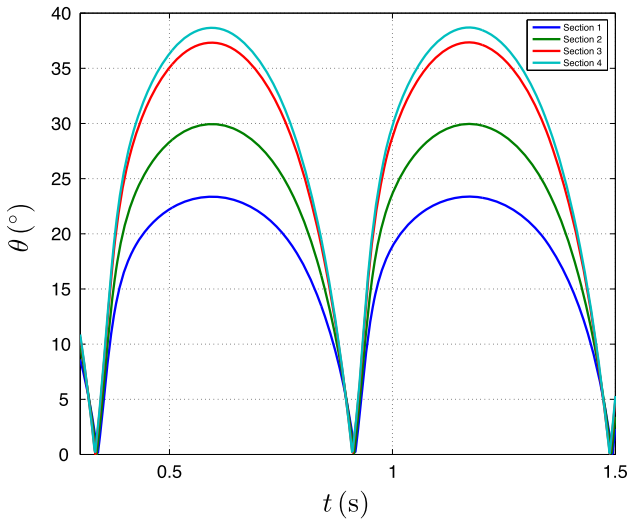

Fig. 14 Time history of the foil twist angle at four cross-sections denoted by Sections 1–4

The experimentally measured data is also plotted in the figures for comparison, and the agreement with the computational results is very good. The averaged drag in the FSI computation is reported in Table 6 and compared with the value given in [46]. The two drag values are very close. These results suggest that the structural response of the foil to hydrodynamic loads, including its twisting motion, is captured very well in the FSI computation. Time history of the twisting angle at Sections 1–4 on the foil are plotted in Fig. 14. As expected, the cross-sections that are further away from the rotation axis twist more. Table 6 summarizes the maximum twist angle for each section predicted by the FSI computation and measured in the experiment. The two data sets match very well, which is further confirmation that the foil twisting action is accurately captured in the FSI simulation. Figure 15 shows the predicted foil configuration at $\theta = 90°$ and $\theta = 0°$ in a side-by-side comparison with the underwater photographs of the foil at the same angular-position instances. This visual comparison reveals very similar deformation patterns between the experimental data and FSI predictions.

Figure 16 shows vorticity isosurfaces colored by flow speed close to the foil surface at two instances during the stroke cycle. The figure illustrates the complexity of the underlying wall-bounded turbulent flow phenomena, and underscores the necessity to use advanced FSI modeling and simulation for this problem class.

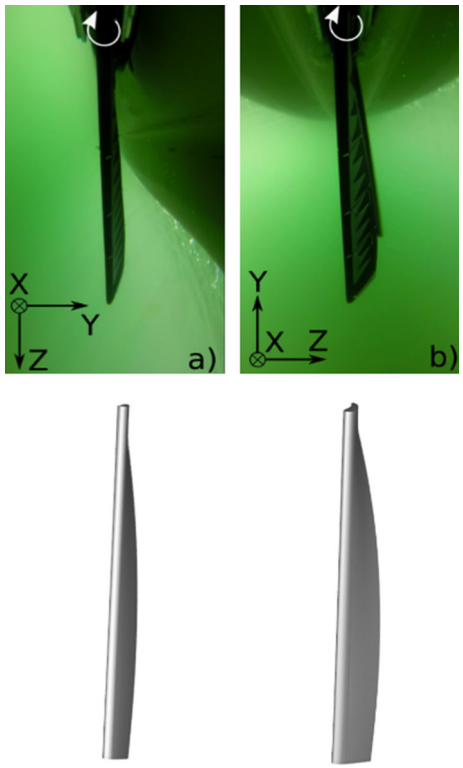

Fig. 15 Foil configuration at $\theta = 90°$ (*left*) and $\theta = 0°$ (*right*). Comparison between the underwater photographs (*top*) and FSI results (*bottom*) at the same angular-positions shows good agreement

4 Conclusions

In this paper, we described an original experimental set up developed to study the Mirage Drive propulsion system based on two oscillating foils in a tandem configuration. Measurements of the foil hydrodynamic moment and twisting deformation are performed for different kayak speeds. The study of thrust performance shows a linear increase of the propulsive efficiency with the boat speed and stroke frequency within the range of the parameters examined. The details of the foil deformation during operation were captured using an underwater camera and a twist-angle calibration system.

FSI simulation of a singe foil was conducted wherein a NURBS-based isogeometric shell model of the foil structure was built and validated through a sag test. A quasi-direct FSI coupling strategy is employed to address the challenges associated with the large added mass present in the coupled system. Excellent agreement in the thrust force, hydrodynamic moment, and foil twist angle is achieved between the experimental measurements and the FSI computation.

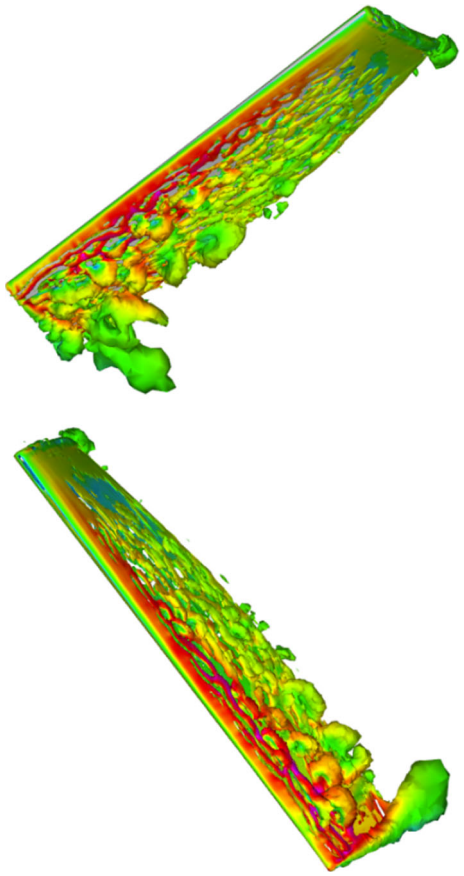

Fig. 16 Vorticity isosurfaces colored by flow speed at two instants during the stroke cycle

Further gains in propulsive efficiency may be obtained by improving the geometric and structural design of the foils. The 3D FSI technique described is able to capture the essential mechanics of the propulsion system, and may be employed in the foil design process in the future.

Acknowledgments J. Yan and Y. Bazilevs were partially supported by the NSF CAREER Award OCI-1055091.

References

1. Augier B, Bot P, Hauville F, Durand M (2012) Experimental validation of unsteady models for fluid structure interaction: application to yacht sails and rigs. J Wind Eng Ind Aerodyn 101:53–66
2. Augier B, Bot P, Hauville F, Durand M (2013) Dynamic behavior of a flexible yacht sail plan. Ocean Eng 66:32–43
3. Bazilevs Y, Calo VM, Hughes TJR, Zhang Y (2008) Isogeometric fluid–structure interaction: theory, algorithms, and computations. Comput Mech 43:3–37
4. Bazilevs Y, Hsu M-C, Akkerman I, Wright S, Takizawa K, Henicke B, Spielman T, Tezduyar TE (2011) 3D simulation of wind turbine rotors at full scale. Part I: geometry modeling and aerodynamics. Int J Numer Methods Fluids 65:207–235
5. Bazilevs Y, Hsu M-C, Benson D, Sankaran S, Marsden A (2009) Computational fluid–structure interaction: methods and application to a total cavopulmonary connection. Comput Mech 45:77–89
6. Bazilevs Y, Hsu M-C, Kiendl J, Wüchner R, Bletzinger K-U (2011) 3D simulation of wind turbine rotors at full scale. Part II: fluid–structure interaction modeling with composite blades. Int J Numer Methods Fluids 65:236–253
7. Bazilevs Y, Hsu M-C, Scott MA (2012) Isogeometric fluid–structure interaction analysis with emphasis on non-matching discretizations, and with application to wind turbines. Comput Methods Appl Mech Eng 249–252:28–41
8. Bazilevs Y, Hsu M-C, Takizawa K, Tezduyar TE (2012) ALE–VMS and ST-VMS methods for computer modeling of wind-turbine rotor aerodynamics and fluid–structure interaction. Math Models Methods Appl Sci 22(supp02):1230002
9. Bazilevs Y, Hsu M-C, Zhang Y, Wang W, Kvamsdal T, Hentschel S, Isaksen J (2010) Computational fluid–structure interaction: methods and application to cerebral aneurysms. Biomech Model Mechanobiol 9:481–498
10. Bazilevs Y, Hsu M-C, Zhang Y, Wang W, Liang X, Kvamsdal T, Brekken R, Isaksen J (2010) A fully-coupled fluid–structure interaction simulation of cerebral aneurysms. Comput Mech 46:3–16
11. Bazilevs Y, Hughes TJR (2007) Weak imposition of Dirichlet boundary conditions in fluid mechanics. Comput Fluids 36:12–26
12. Bazilevs Y, Hughes TJR (2008) NURBS-based isogeometric analysis for the computation of flows about rotating components. Comput Mech 43:143–150
13. Bazilevs Y, Korobenko A, Deng X, Yan J, Kinzel M, Dabiri JO (2014) Fluid–structure interaction modeling of vertical-axis wind turbines. J Appl Mech 81(8):081006
14. Bazilevs Y, Michler C, Calo VM, Hughes TJR (2007) Weak Dirichlet boundary conditions for wall-bounded turbulent flows. Comput Methods Appl Mech Eng 196:4853–4862
15. Bazilevs Y, Michler C, Calo VM, Hughes TJR (2010) Isogeometric variational multiscale modeling of wall-bounded turbulent flows with weakly enforced boundary conditions on unstretched meshes. Comput Methods Appl Mech Eng 199:780–790
16. Bazilevs Y, Takizawa K, Tezduyar TE (2013) Challenges and directions in computational fluid–structure interaction. Math Models Methods Appl Sci 23:215–221
17. Bazilevs Y, Takizawa K, Tezduyar TE (2013) Computational fluid–structure interaction: methods and applications. Wiley, New York
18. Belytschko T, Liu WK, Moran B (2000) Nonlinear finite elements for continua and structures. Wiley, Chichester
19. Chung J, Hulbert GM (1993) A time integration algorithm for structural dynamics withimproved numerical dissipation: the generalized-α method. J Appl Mech 60:371–375
20. Combes SA, Daniel TL (2001) Shape, flapping and flexion: wing and fin design for forward flight. J Exp Biol 204(12):2073–2085
21. Cottrell JA, Hughes TJR, Bazilevs Y (2009) Isogeometric analysis: toward integration of CAD and FEA. Wiley, Chichester
22. Dabiri JO (2011) Potential order-of-magnitude enhancement of wind farm power density via counter-rotating vertical-axis wind turbine arrays. J Renew Sustain Energy 3:043104
23. Fish FE (1999) Performance constraints on the maneuverability of flexible and rigid biological systems. In: International symposium on unmanned unthethered submersible technology, University of New Hampshire-Marine Systems, 1999, pp 394–406
24. Hsu M-C, Akkerman I, Bazilevs Y (2011) High-performance computing of wind turbine aerodynamics using isogeometric analysis. Comput Fluids 49:93–100
25. Hsu M-C, Akkerman I, Bazilevs Y (2012) Wind turbine aerodynamics using ALE–VMS: validation and the role of weakly enforced boundary conditions. Comput Mech 50:499–511. doi:10.1007/s00466-012-0686-x

26. Hsu M-C, Akkerman I, Bazilevs Y (2014) Finite element simulation of wind turbine aerodynamics: validation study using NREL Phase VI experiment. Wind Energy 17:461–481
27. Hsu M-C, Bazilevs Y (2011) Blood vessel tissue prestress modeling for vascular fluid–structure interaction simulations. Finite Elem Anal Des 47:593–599
28. Hsu M-C, Bazilevs Y (2012) Fluid–structure interaction modeling of wind turbines: simulating the full machine. Comput Mech 50:821–833
29. Hughes TJR, Cottrell JA, Bazilevs Y (2005) Isogeometric analysis: CAD, finite elements, NURBS, exact geometry, and mesh refinement. Comput Methods Appl Mech Eng 194:4135–4195
30. Hughes TJR, Liu WK, Zimmermann TK (1981) Lagrangian–Eulerian finite element formulation for incompressible viscous flows. Comput Methods Appl Mech Eng 29:329–349
31. Jansen KE, Whiting CH, Hulbert GM (2000) A generalized-α method for integrating the filtered Navier–Stokes equations with a stabilized finite element method. Comput Methods Appl Mech Eng 190:305–319
32. Johnson AA, Tezduyar TE (1994) Mesh update strategies in parallel finite element computations of flow problems with moving boundaries and interfaces. Comput Methods Appl Mech Eng 119:73–94
33. Karypis G, Kumar V (1999) A fast and high quality multilevel scheme for partitioning irregular graphs. SIAM J Sci Comput 20:359–392
34. Kiendl J, Bazilevs Y, Hsu M-C, Wüchner R, Bletzinger K-U (2010) The bending strip method for isogeometric analysis of Kirchhoff–Love shell structures comprised of multiple patches. Comput Methods Appl Mech Eng 199:2403–2416
35. Kiendl J, Bletzinger K-U, Linhard J, Wüchner R (2009) Isogeometric shell analysis with Kirchhoff–Love elements. Comput Methods Appl Mech Eng 198:3902–3914
36. Koochesfahani MM (1989) Vortical patterns in the wake of an oscillating airfoil. AIAA J 27(9):1200–1205
37. Korobenko A, Hsu M-C, Akkerman I, Bazilevs Y (2013) Aerodynamic simulation of vertical-axis wind turbines. J Appl Mech 81(2):021011
38. Korobenko A, Hsu MC, Akkerman I, Tippmann J, Bazilevs Y (2013) Structural mechanics modeling and fsi simulation of wind turbines. Math Models Methods Appl Sci 23:249–272
39. Lai SJC, Platzer MF (1999) Jet characteristics of a plunging airfoil. AIAA J 37(12):1529–1537
40. Leroyer A, Visonneau M (2005) Numerical methods for RANSE simulations of a self-propelled fish-like body. J Fluids Struct 20(7):975–991
41. Long CC, Esmaily-Moghadam M, Marsden AL, Bazilevs Y (2014) Computation of residence time in the simulation of pulsatile ventricular assist devices. Comput Mech 54:911–919
42. Long CC, Hsu M-C, Bazilevs Y, Feinstein JA, Marsden AL (2012) Fluid–structure interaction simulations of the Fontan procedure using variable wall properties. Int J Numer Methods Biomed Eng 28:512–527
43. Long CC, Marsden AL, Bazilevs Y (2013) Fluid–structure interaction simulation of pulsatile ventricular assist devices. Comput Mech 52:971–981
44. Long CC, Marsden AL, Bazilevs Y (2014) Shape optimization of pulsatile ventricular assist devices using FSI to minimize thrombotic risk. Comput Mech 54:921–932
45. Mountcastle AM, Daniel TL (2009) Aerodynamic and functional consequences of wing compliance. Exp Fluid 46(5):873–882
46. Peters T (2010) Hobie kayak mirage drive tow tank testing. Report: Departement of Naval Architecture & Marine Engineering, University of Michigan 1:1–7
47. Raknes SB, Deng X, Bazilevs Y, Benson DJ, Mathisen KM, Kvamsdal T (2013) Isogeometric rotation-free bending-stabilized cables: statics, dynamics, bending strips and coupling with shells. Comput Methods Appl Mech Eng 263:127–143
48. Read DA, Hover FS, Triantafyllou MS (2003) Forces on oscillating foils for propulsion and maneuvering. J Fluids Struct 17(1):163–183
49. Schouveiler L, Hover FS, Triantafyllou MS (2005) Performance of flapping foil propulsion. J Fluids Struct 20(7):949–959
50. Shyy W, Aono H, Chimakurthi SK, Trizila P, Kang CK, Cesnik CES, Liu H (2010) Recent progress in flapping wing aerodynamics and aeroelasticity. Prog Aerosp Sci 46(7):284–327
51. Stein K, Tezduyar T, Benney R (2003) Mesh moving techniques for fluid–structure interactions with large displacements. J Appl Mech 70:58–63
52. Suito H, Takizawa K, Huynh VQH, Sze D, Ueda T (2014) FSI analysis of the blood flow and geometrical characteristics in the thoracic aorta. Comput Mech 54:1035–1045
53. Takizawa K (2014) Computational engineering analysis with the new-generation space–time methods. Comput Mech 54:193–211
54. Takizawa K, Bazilevs Y, Tezduyar TE (2012) Space–time and ALE–VMS techniques for patient-specific cardiovascular fluid–structure interaction modeling. Arch Comput Methods Eng 19:171–225
55. Takizawa K, Bazilevs Y, Tezduyar TE, Long CC, Marsden AL, Schjodt K (2014) ST and ALE–VMS methods for patient-specific cardiovascular fluid mechanics modeling. Math Models Methods Appl Sci 24:2437–2486
56. Takizawa K, Christopher J, Tezduyar TE, Sathe S (2010) Space–time finite element computation of arterial fluid–structure interactions with patient-specific data. Int J Numer Methods Biomed Eng 26:101–116
57. Takizawa K, Henicke B, Puntel A, Kostov N, Tezduyar TE (2012) Space–time techniques for computational aerodynamics modeling of flapping wings of an actual locust. Comput Mech 50:743–760
58. Takizawa K, Henicke B, Puntel A, Kostov N, Tezduyar TE (2013) Computer modeling techniques for flapping-wing aerodynamics of a locust. Comput Fluids 85:125–134
59. Takizawa K, Kostov N, Puntel A, Henicke B, Tezduyar TE (2012) Space–time computational analysis of bio-inspired flapping-wing aerodynamics of a micro aerial vehicle. Comput Mech 50:761–778
60. Takizawa K, Montes D, Fritze M, McIntyre S, Boben J, Tezduyar TE (2013) Methods for FSI modeling of spacecraft parachute dynamics and cover separation. Math Models Methods Appl Sci 23:307–338
61. Takizawa K, Montes D, McIntyre S, Tezduyar TE (2013) Space–time VMS methods for modeling of incompressible flows at high Reynolds numbers. Math Models Methods Appl Sci 23:223–248
62. Takizawa K, Moorman C, Wright S, Purdue J, McPhail T, Chen PR, Warren J, Tezduyar TE (2011) Patient-specific arterial fluid–structure interaction modeling of cerebral aneurysms. Int J Numer Methods Fluids 65:308–323
63. Takizawa K, Schjodt K, Puntel A, Kostov N, Tezduyar TE (2013) Patient-specific computational analysis of the influence of a stent on the unsteady flow in cerebral aneurysms. Comput Mech 51:1061–1073
64. Takizawa K, Spielman T, Tezduyar TE (2011) Space–time FSI modeling and dynamical analysis of spacecraft parachutes and parachute clusters. Comput Mech 48:345–364
65. Takizawa K, Takagi H, Tezduyar TE, Torii R (2014) Estimation of element-based zero-stress state for arterial FSI computations. Comput Mech 54:895–910
66. Takizawa K, Tezduyar TE (2011) Multiscale space–time fluid–structure interaction techniques. Comput Mech 48:247–267
67. Takizawa K, Tezduyar TE (2012) Computational methods for parachute fluid–structure interactions. Arch Comput Methods Eng 19:125–169

68. Takizawa K, Tezduyar TE (2012) Space–time fluid–structure interaction methods. Math Models Methods Appl Sci 22(supp02): 1230001
69. Takizawa K, Tezduyar TE, Boben J, Kostov N, Boswell C, Buscher A (2013) Fluid–structure interaction modeling of clusters of spacecraft parachutes with modified geometric porosity. Comput Mech 52:1351–1364
70. Takizawa K, Tezduyar TE, Boswell C, Kolesar R, Montel K (2014) FSI modeling of the reefed stages and disreefing of the Orion spacecraft parachutes. Comput Mech 54:1203–1220
71. Takizawa K, Tezduyar TE, Buscher A, Asada S (2014) Space–time fluid mechanics computation of heart valve models. Comput Mech 54:973–986
72. Takizawa K, Tezduyar TE, Buscher A, Asada S (2014) Space–time interface-tracking with topology change (ST-TC). Comput Mech 54:955–971
73. Takizawa K, Tezduyar TE, Kolesar R, Boswell C, Kanai T, Montel K (2014) Multiscale methods for gore curvature calculations from FSI modeling of spacecraft parachutes. Comput Mech, published online, doi:10.1007/s00466-014-1069-2
74. Takizawa K, Tezduyar TE, Kostov N (2014) Sequentially-coupled space–time FSI analysis of bio-inspired flapping-wing aerodynamics of an MAV. Comput Mech 54:213–233
75. Takizawa K, Tezduyar TE, McIntyre S, Kostov N, Kolesar R, Habluetzel C (2014) Space–time VMS computation of wind-turbine rotor and tower aerodynamics. Comput Mech 53:1–15
76. Takizawa K, Torii R, Takagi H, Tezduyar TE, Xu XY (2014) Coronary arterial dynamics computation with medical-image-based time-dependent anatomical models and element-based zero-stress state estimates. Comput Mech 54:1047–1053
77. Takizawa K, Wright S, Moorman C, Tezduyar TE (2011) Fluid–structure interaction modeling of parachute clusters. Int J Numer Methods Fluids 65:286–307
78. Tezduyar T, Aliabadi S, Behr M, Johnson A, Mittal S (1993) Parallel finite-element computation of 3D flows. Computer 26(10):27–36
79. Tezduyar TE (2001) Finite element methods for flow problems with moving boundaries and interfaces. Arch Comput Methods Eng 8:83–130
80. Tezduyar TE, Behr M, Mittal S, Johnson AA (1992) Computation of unsteady incompressible flows with the finite element methods - space–time formulations, iterative strategies and massively parallel implementations. In: New Methods in Transient Analysis, PVP-Vol. 246/AMD-Vol.143. ASME, New York, 1992, pp 7–24
81. Tezduyar TE, Sathe S (2007) Modeling of fluid–structure interactions with the space–time finite elements: solution techniques. Int J Numer Methods Fluids 54:855–900
82. Tezduyar TE, Sathe S, Keedy R, Stein K (2004) Space-time techniques for finite element computation of flows with moving boundaries and interfaces. In: Gallegos S, Herrera I, Botello S, Zarate F, Ayala G (eds) Proceedings of the III international congress on numerical methods in engineering and applied science. CD-ROM, Monterrey, Mexico
83. Tezduyar TE, Sathe S, Keedy R, Stein K (2006) Space–time finite element techniques for computation of fluid–structure interactions. Comput Methods Appl Mech Eng 195:2002–2027
84. Tezduyar TE, Sathe S, Pausewang J, Schwaab M, Christopher J, Crabtree J (2008) Interface projection techniques for fluid–structure interaction modeling with moving-mesh methods. Comput Mech 43:39–49
85. Tezduyar TE, Sathe S, Stein K (2006) Solution techniques for the fully-discretized equations in computation of fluid–structure interactions with the space-time formulations. Comput Methods Appl Mech Eng 195:5743–5753
86. Tezduyar TE, Schwaab M, Sathe S (2009) Sequentially-coupled arterial fluid–structure interaction (SCAFSI) technique. Comput Methods Appl Mech Eng 198:3524–3533
87. Tezduyar TE, Takizawa K, Brummer T, Chen PR (2011) Space–time fluid–structure interaction modeling of patient-specific cerebral aneurysms. Int J Numer Methods Biomed Eng 27:1665–1710
88. Tezduyar TE, Takizawa K, Moorman C, Wright S, Christopher J (2010) Multiscale sequentially-coupled arterial FSI technique. Comput Mech 46:17–29
89. Tezduyar TE, Takizawa K, Moorman C, Wright S, Christopher J (2010) Space–time finite element computation of complex fluid–structure interactions. Int J Numer Methods Fluids 64:1201–1218
90. Wakeling JM, Ellington CP (1997) Dragonfly flight. ii. velocities, accelerations and kinematics of flapping flight. J Exp Biol 200(3):557–582
91. Wang ZJ, Russell D (2007) Effect of forewing and hindwing interactions on aerodynamic forces and power in hovering dragonfly flight. Phys Rev Lett 99(14):148101